minerals

MDPI

Article

Geochemical Characteristics and Geological Significance of Black Shale at the Bottom of the Mufushan Formation in the Lower Cambrian, Lower Yangtze Platform, South China

Jiaqi Li [1], Zhihong Kang [1,*], Zhijiang Kang [2] and Xuemei Zhang [3]

[1] School of Energy Resources, China University of Geosciences, Beijing 100083, China; lijiaqi0527@foxmail.com
[2] SINOPEC Exploration and Production Research Institute, Beijing 100083, China; kangzj.syky@sinopec.com
[3] School of Geosciences, China University of Petroleum, Qingdao 266580, China; 15532171545@163.com
* Correspondence: kangzh98@cugb.edu.cn

Abstract: Black shale, as an important unconventional energy resource, has attracted significant attention in recent years. By studying its sedimentary and geochemical characteristics, it is possible to reconstruct ancient depositional environments and paleoclimatic conditions. The Lower Cambrian black shale is widely distributed in the Lower Yangtze region, but its tectonic background and provenance have been subject to debate. In this study, we conducted geochemical testing and analysis on samples collected from the basal black shale of the Mufushan Formation in the Mufushan section, Nanjing. The Th/Sc-Zr/Sc diagram indicates that the black shale of the Mufushan Formation has not undergone sedimentary recycling. Analysis of major element ratios, rare earth element (REE) distribution patterns, δEu, (La/Yb)N, and the La/Th-Hf and La/Yb-∑REE discrimination diagrams suggest that the source rocks of the black shale mainly consist of granites and sedimentary rocks rich in ferromagnesian minerals, representing felsic rocks derived from the upper crust, with some involvement of mafic rocks. Considering the provenance attributes, geological age relationships, and tectonic evolution of the South China continent, the granite component in the source rocks is inferred to have formed during Neoproterozoic magmatic activity, and the source area corresponds to the Jiangnan Orogenic Belt. Analysis of $K_2O + Na_2O$-SiO_2, K_2O/Na_2O-SiO_2/Al_2O_3, La-Th-Sc, Th-Co-Zr/10, and Th-Sc-Zr/10 diagrams suggests that the source area of the Mufushan Formation black shale was a passive continental margin.

Keywords: black shale; Lower Yangtze region; Lower Cambrian; element geochemistry; palaeoenvironment

check for updates

Citation: Li, J.; Kang, Z.; Kang, Z.; Zhang, X. Geochemical Characteristics and Geological Significance of Black Shale at the Bottom of the Mufushan Formation in the Lower Cambrian, Lower Yangtze Platform, South China. *Minerals* **2023**, *13*, 1095. https://doi.org/10.3390/min13081095

Academic Editor: János Haas

Received: 5 July 2023
Revised: 11 August 2023
Accepted: 15 August 2023
Published: 16 August 2023

1. Introduction

The term "black shale" refers to fine-grained sedimentary rocks, as well as their associated lithologies, that contain a significant amount of organic carbon, resulting in their characteristic black coloration. The black shale series primarily includes various types of shale, chert, and siltstone, among others [1]. Because of their high organic content, these rocks are potential hydrocarbon source rocks, as well as valuable records of past environmental conditions.

The period from the pre-Cambrian to the early Cambrian (equivalent to the Ediacaran to early Cambrian) represents a crucial time in global tectonic activity and sedimentary environmental changes [2–6]. It was characterized by the breakup and dispersal of the Rodinia supercontinent, the assembly of the Gondwana supercontinent [3,7–20], as well as associated events such as widespread marine transgressions, hydrothermal activities, and episodes of persistent oceanic anoxia [21–28]. These events had a significant impact on the co-evolution of global geological environments and biota, leading to the widespread distribution of Lower Cambrian black shales. Previous research has indicated that the formation of black shale is facilitated by rapid marine transgressions, oceanic salinity stratification, stagnant water conditions, high biological productivity, extensive organic matter decomposition, and seafloor hydrothermal activity [22,29–46]. However, the coupling relationship between the genesis of black shales and their depositional environment remains a subject of ongoing debate.

The Lower Cambrian black shale series is widely distributed in southern China, and recent research, focusing on the Lower Cambrian Mufushan Formation in the Yangtze region, has revealed the distribution and geochemical characteristics of these black shale formations. Studies by Wu et al. [25,44,47–49] propose that the deposition of black shale in the Mufushan Formation may have been influenced by the influx of terrigenous sediments from adjacent magmatic arcs during the Neoproterozoic-Mesoproterozoic period. This hypothesis suggests a potential connection between tectonic activity and the deposition of organic-rich black shales in the Yangtze region. However, little is known about the sources of organic matter and the tectonic environment influencing its deposition in the study area.

Addressing these scientific questions is crucial for a comprehensive understanding of the formation process and geological significance of black shales in the Mufushan Formation. Therefore, this study conducted detailed geological and geochemical analyses on samples collected from the lowermost layer of the Mufushan Formation in the Yangtze region. By integrating data from various analytical techniques, including Th/Sc-Zr/Sc diagrams, elemental ratios, and rare earth element (REE) patterns, we aimed to identify the provenance of the sedimentary rocks and to determine the tectonic environment, thus providing valuable insights into the geological evolution of the Yangtze region during the early Cambrian. It lays the foundation for further research on organic-rich black shale formations and their potential as hydrocarbon reservoirs. Moreover, it advances our understanding of the processes governing sedimentary environments and reveals the complex interactions between tectonic and depositional processes in ancient marine basins.

2. Geological Setting

The Lower Yangtze region generally refers to the area within the lower reaches of the Yangtze River in the Yangtze Plate, with its western and northwest boundaries defined by the Tan-Lu Fault and Jiaoshan-Xiangshui Fault, and its southwestern boundary extending to Jiujiang, adjacent to the Middle Yangtze region delineated by the Ganjiang Fault. To the south and southeast, it is bounded by the Jiangshao Fault, adjacent to the Huaxia Plate, and extends eastward to the southern Yellow Sea (Figure 1). The area covers an approximate area of 3.6×10^5 km^2 [37,47–49].

The Lower Yangtze region is a superimposed basin that has experienced multiple tectonic events, resulting in a complex structural pattern. It can be divided into two major stages of tectonic evolution: marine basin evolution and continental basin evolution, roughly separated by the Middle-Late Triassic. From the Cambrian to the early Paleozoic, the Lower Yangtze region exhibited a sedimentary pattern known as the "two basins sandwiching one platform". The central platform is primarily composed of carbonate sedimentation, while the deeper water basins on both sides are characterized by the development of organic-rich black shales and cherts [13,46,50].

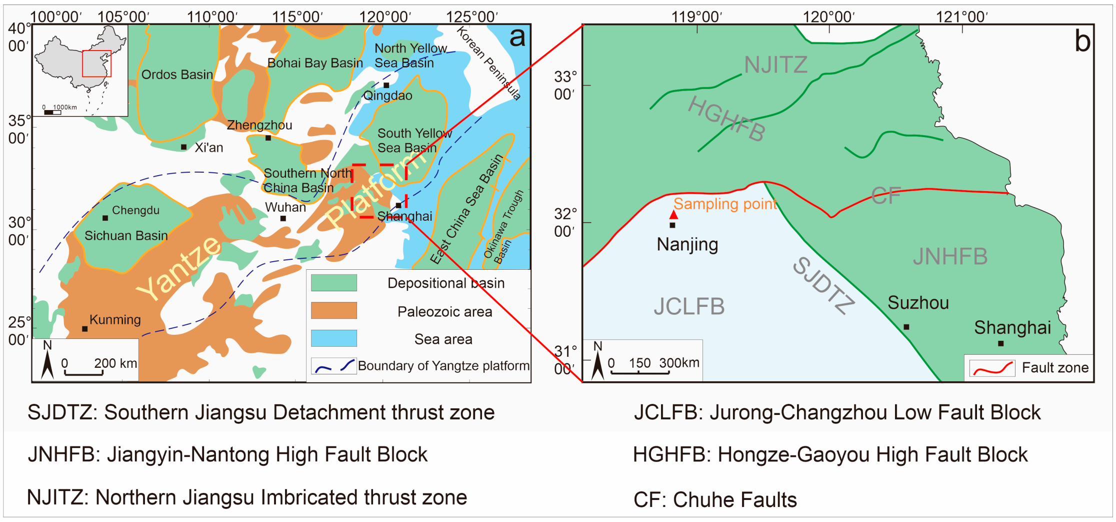

Figure 1. (**a**) Location of Yangtze Platform; (**b**) Division of geotectonic system unit of study areas (modified from [51]).

3. Samples and Methods

The samples used in this study were fresh black shale and mudstone samples collected during fieldwork. The sampling location was the Mufushan section in Nanjing City, Jiangsu Province, China (32°07′11.06″ N, 118°47′06.84″ E) (Figure 1b). The samples were obtained from the lowermost part of the Mufushan Formation (Figures 2 and 3). The lithology of the Mufushan Formation can be divided into two parts: the lower part consists of a black shale series with interbedded dolomitic mudstones, while the upper part consists of a thick sequence of dolomites with interbedded purple and black mudstones, unconformably overlain by the Dengying Formation.

Figure 2. The outcrop of the bottom of the Cambrian Mufushan Formation in the Mufushan section of Nanjing.

The sample analyses were conducted at the Analysis and Testing Center of the Beijing Research Institute of Uranium Geology, which is affiliated with the Nuclear Industry Beijing Geological Research Institute. For the analysis of total organic carbon (TOC), the shale samples were first crushed and ground to a particle size greater than 200 mesh. The powdered sample was then treated with hydrochloric acid (analytically pure HCl:water = 1:7) and maintained at temperatures between 60 and 80 °C for two hours to ensure complete dissolution of carbonate minerals. After this process, the remaining material was rinsed with distilled water to achieve a neutral pH and then dried at 100 °C. Subsequently, the samples were analyzed using a CS-230 Carbon-Sulfur analyzer (LECO). The total organic carbon (TOC) contents are reported as weight percentage (wt%), accounting for the material lost during the acid treatment. The analytical uncertainty is less than 0.5%.

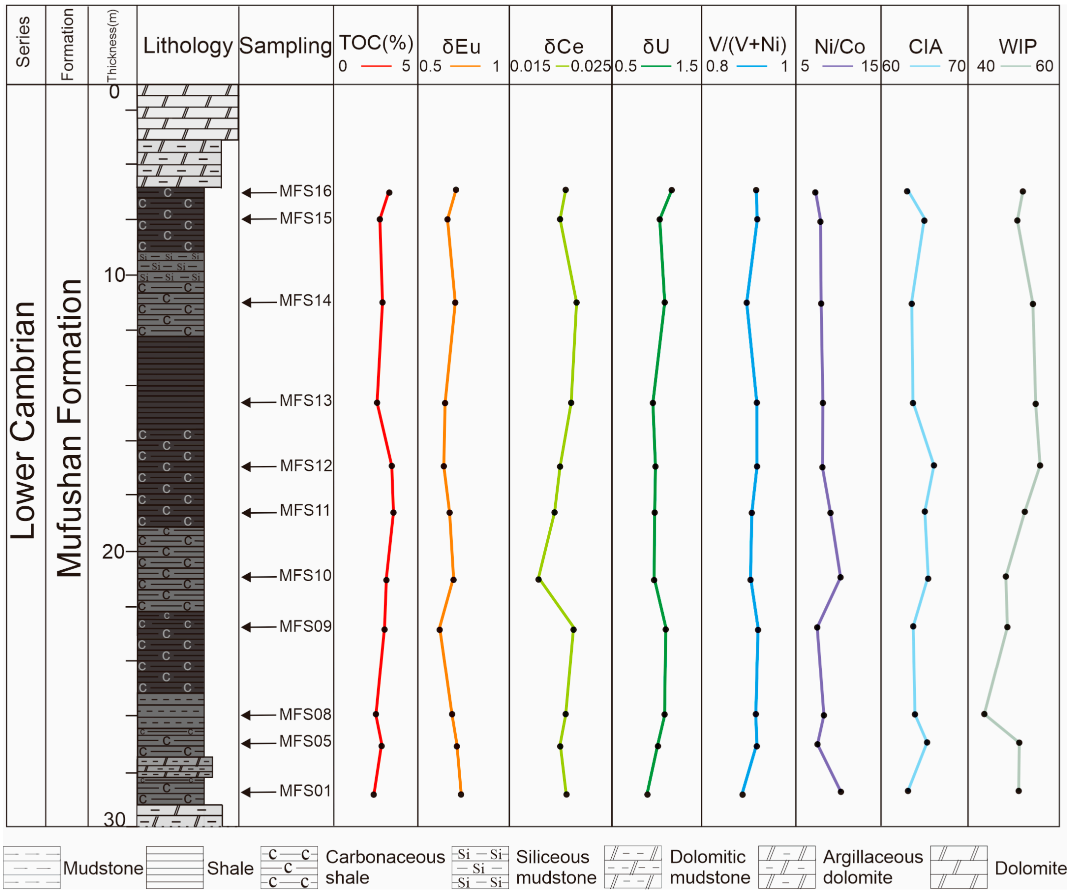

Figure 3. Lithology and sample locations within the lower Mufushan Formation in the Mufushan section. The line chart shows the variations of TOC content and paleosedimentary-related inorganic geochemical parameters with depth. The parameters include V/V + Ni, Ni/Co, and δU, which serve as indicators of paleoredox conditions. CIA and WIP are used as indicators of weathering intensity. CIA = Chemical Index of Alteration; WIP = Weathering Index.

Major elements were measured using a wavelength scanning X-ray fluorescence spectrometer (XRF) RIX-2100. Trace elements were analyzed using an inductively coupled plasma mass spectrometer (ICP-MS) NexION 300Q. The sample preparation process for ICP-MS analysis included the following steps: Approximately 50 mg of crushed rock powder with a particle size of about 200 mesh was weighed and placed in a Teflon-sealed digestion vessel. The samples were digested using acid solution (HF + HNO_3) at 195 °C for 48 h. After Si removal at 120 °C, the samples were diluted 2000 times with 2% HNO_3 and then transferred to clean polyethylene bottles for analysis.

4. Results

4.1. Total Organic Carbon (TOC) Characteristics

The results of total organic carbon (TOC) are presented in Figure 3. The lower black shale series exhibits a relatively high total organic carbon (TOC) content. A total of 11 fresh samples were collected, with TOC ranging from 2.29% to 3.88%, averaging at 3.05%. Across samples MFS-01 to MFS-12, an upward trend in TOC content is observed from bottom to top. The highest TOC content is recorded in sample MFS-12, reaching 3.88%. Subsequently, a decrease in TOC content is noted in sample MFS-13, followed by a rise to 3.55% in sample MFS-16. Overall, the data delineate two distinct upward shifts in TOC content.

4.2. Major Element Characteristics

The results of major element analysis are presented in Table 1. The SiO_2 content ranges from 68.430% to 73.160%, with an average of 71.887%. The Al_2O_3 content ranges from 10.130% to 13.960%, with an average of 11.842%. The $Fe_2O_3{}^T$ (total iron expressed as Fe_2O_3) content ranges from 1.479% to 7.498%, with an average of 2.769%. The MgO content ranges from 0.645% to 0.847%, with an average of 0.719%. The CaO content ranges from 0.113% to 0.262%, with an average of 0.154%. The TiO_2 content ranges from 0.560% to 0.793%, with an average of 0.650%. The MnO content ranges from 0.007% to 0.013%, with an average of 0.009%. The P_2O_5 content ranges from 0.124% to 0.592%, with an average of 0.278%. The Na_2O content ranges from 0.067% to 0.199%, with an average of 0.113%. The K_2O content ranges from 4.940% to 6.110%, with an average of 5.721%.

Table 1. Major element data for the black shale series of the Mufushan Formation at the Mufushan section (units are wt%).

Major Element	MFS-01	MFS-05	MFS-08	MFS-09	MFS-10	MFS-11	MFS-12	MFS-13	MFS-14	MFS-15	MFS-16	PAAS
SiO_2	73.160	71.920	70.760	72.390	72.500	71.000	68.430	72.700	72.800	73.020	72.080	62.800
Al_2O_3	10.900	12.430	10.130	11.370	12.010	12.390	13.960	11.960	11.820	12.040	11.250	18.900
Fe_2O_3	1.430	1.380	6.520	1.770	1.200	1.320	1.290	1.280	1.040	1.100	1.990	7.220
MgO	0.655	0.806	0.645	0.719	0.756	0.741	0.847	0.721	0.645	0.676	0.699	2.200
CaO	0.130	0.150	0.138	0.140	0.154	0.262	0.221	0.130	0.113	0.123	0.130	1.300
Na_2O	0.067	0.118	0.123	0.199	0.108	0.099	0.116	0.102	0.101	0.098	0.116	1.200
K_2O	5.780	5.640	4.940	5.470	5.420	5.820	6.100	6.110	6.080	5.660	5.910	3.700
MnO	0.009	0.007	0.008	0.010	0.009	0.011	0.008	0.009	0.009	0.008	0.013	0.110
TiO_2	0.612	0.657	0.560	0.637	0.674	0.705	0.793	0.651	0.633	0.648	0.581	1.000
P_2O_5	0.256	0.149	0.512	0.592	0.404	0.214	0.083	0.124	0.132	0.115	0.480	0.160
loss on ignition	6.750	6.640	6.300	6.980	6.950	7.650	8.710	6.510	6.480	6.700	6.580	6.000
FeO	1.080	1.000	0.880	1.050	0.890	0.250	0.170	1.020	0.870	0.660	1.260	
K_2O/Na_2O	86.269	47.797	40.163	27.487	50.185	58.788	52.586	59.902	60.198	57.755	50.948	3.083
$Fe_2O_3 + MgO$	2.085	2.186	7.165	2.489	1.956	2.061	2.137	2.001	1.685	1.776	2.689	9.420
Al_2O_3/SiO_2	0.149	0.173	0.143	0.157	0.166	0.175	0.204	0.165	0.162	0.165	0.156	0.301
$K_2O/(Na_2O + CaO)$	29.340	21.045	18.927	16.136	20.687	16.122	18.101	26.336	28.411	25.611	24.024	1.480
$Al_2O_3/(CaO + Na_2O)$	55.330	46.381	38.812	33.540	45.840	34.321	41.424	51.552	55.234	54.480	45.732	7.560
$Fe_2O_3 + MgO$	2.085	2.186	7.165	2.489	1.956	2.061	2.137	2.001	1.685	1.776	2.689	9.420
$K_2O + Na_2O$	5.847	5.758	5.063	5.669	5.528	5.919	6.216	6.212	6.181	5.758	6.026	4.900
$\log(K_2O + Na_2O)$	0.767	0.760	0.704	0.754	0.743	0.772	0.794	0.793	0.791	0.760	0.780	0.690
SiO_2/Al_2O_3	0.173	0.177	0.202	0.183	0.185	0.172	0.164	0.164	0.164	0.177	0.169	3.323
$Fe_2O_3{}^T$	2.630	2.491	7.498	2.937	2.189	1.598	1.479	2.413	2.007	1.833	3.390	7.220
CIA	62.6	65.6	63.7	63.3	65.8	65.1	66.6	63.2	63.0	65.1	62.3	70.356
WIP	51.102	51.209	43.603	48.756	48.261	52.453	55.622	54.859	54.313	50.879	52.031	51.440

Note: $Fe_2O_3{}^T$ represents total iron content expressed as Fe_2O_3; PAAS values are from Mc Lennan (1985) [52]; CIA = Chemical Index of Alteration; WIP = Weathering Index.

Comparing the elemental composition of the lower part of the black shale series in the Mufushan section with the Australian Post-Archean Average Shale (PAAS), it is observed that the Mufushan section exhibits enrichment in SiO_2, K_2O, and P_2O_5, while depletion in Al_2O_3, $Fe_2O_3{}^T$, MgO, CaO, TiO_2, P_2O_5, and Na_2O.

4.3. Characteristics of Trace Elements

The results of trace element analysis are presented in Table 2. The trace elements of the samples, standardized against the Australian Post-Archean Average Shale (PAAS), are shown in Figure 4a. With the exception of Cr, Sr, and Ba, which are comparable to PAAS, all other trace elements exhibit varying degrees of depletion. Strong depletions are observed for elements such as Co, Ni, Cu, and Zn.

Table 2. Trace element and rare earth element (REE) data for the black shales of the Mufushan Formation at the Mufushan section (units are µg/g).

Trace and Rare Earth Elements	MFS-01	MFS-05	MFS-08	MFS-09	MFS-10	MFS-11	MFS-12	MFS-13	MFS-14	MFS-15	MFS-16
Li	10.4	11.4	11.3	9.66	9.77	8.63	9.37	10.4	10.1	10.7	7.77
Be	1.68	1.83	1.68	1.58	1.71	1.59	2	1.7	1.55	1.6	1.58
Sc	7.95	8.26	8.39	8.14	8.11	8.36	9.15	8.04	8.33	9.83	8.4
V	79.1	71.8	59.4	66.4	69	77.9	88.9	68.5	68.5	67.1	73.9
Cr	101	100	97.9	99.6	103	116	144	95.9	98.3	99.9	113
Co	1.02	0.77	0.98	0.72	0.75	0.79	0.83	0.71	0.7	0.78	0.76
Ni	6.13	5.35	6.9	5.34	5.51	7.05	8.89	4.52	5.47	4.98	10.1
Cu	4.79	3.72	4.6	4.18	3.76	4.22	4.83	4.12	4.95	4.91	8.21
Zn	8.85	8.23	9.68	6.93	7.71	8.08	9.17	7.16	8.63	7.86	33.4
Ga	13.1	14.3	11.9	13.1	13.7	14.2	16.3	13.2	13.9	14.1	14.3
Rb	81.6	91	83.7	85.9	88.1	92.8	104	86.4	89.1	89.4	85.3
Sr	123	91.8	155	105	180	110	105	92.6	164	251	287
Y	12.4	12.2	11.7	11.3	12.3	11.9	13.9	11.2	12.3	12.3	53.9
Mo	3.26	4.63	7.6	8.15	8.78	3.45	4.32	7.31	7.12	5.69	6.42
Cd	0.33	0.03	0.04	0.03	0.02	0.03	0.02	0.02	0.02	0.02	0.1
In	0.04	0.04	0.05	0.04	0.04	0.03	0.03	0.03	0.04	0.03	0.03
Sb	0.52	0.32	0.26	0.26	0.26	0.25	0.33	0.18	0.19	0.24	0.25
Cs	4.78	6.4	4.54	5.92	6.18	6.6	8.5	5.74	5.29	5.49	6.55
Ba	440	419	304	313	385	340	426	280	662	553	546
La	30.2	32	31.3	30.8	34.7	33.8	39.4	30.5	31.3	26.4	34.7
Ce	35.5	39.3	31.8	36.4	39.9	40.1	47.6	36.5	37.2	38.8	42.3
Pr	5.57	6.02	5.02	5.51	6	6.14	7.39	5.42	5.72	5.93	6.1
Nd	19.1	21.1	17.9	18.6	19.9	20.2	24.8	17.7	18.4	20.2	18.8
Sm	2.45	2.71	2.83	2.41	2.4	2.46	3.27	2.06	2.21	2.7	2.56
Eu	0.49	0.48	0.57	0.42	0.42	0.45	0.63	0.35	0.42	0.53	0.53
Gd	1.77	1.88	2.17	1.67	1.72	1.72	2.26	1.48	1.57	1.8	1.78
Tb	0.32	0.33	0.37	0.29	0.3	0.3	0.37	0.26	0.28	0.31	0.34
Dy	1.93	1.95	2.05	1.75	1.8	1.75	2.17	1.62	1.74	1.84	1.08
Ho	0.46	0.46	0.45	0.41	0.45	0.43	0.5	0.39	0.43	0.45	0.46
Er	1.48	1.45	1.39	1.33	1.46	1.4	1.63	1.3	1.43	1.45	1.67
Tm	0.26	0.26	0.23	0.23	0.26	0.25	0.28	0.23	0.25	0.25	0.26
Yb	1.68	1.7	1.51	1.57	1.79	1.67	1.87	1.57	1.71	1.67	1.71
Lu	0.27	0.28	0.24	0.25	0.29	0.27	0.29	0.25	0.27	0.26	0.21
W	1.56	1.51	1.31	1.57	1.66	1.94	2.31	1.45	1.66	1.54	1.78
Re	0.21	0.01	0.04	0.01	0.01	0.01	0.01	0.01	0	0.01	0.01
Tl	2.51	2.46	1.73	1.82	1.79	1.64	1.66	1.75	1.79	2.1	2.73
Pb	18	17.3	17.3	14.2	13.1	12.8	14.3	14.4	15	14.8	14.8
Bi	0.41	0.17	0.15	0.15	0.16	0.13	0.14	0.14	0.15	0.16	0.13
Th	5.02	5.1	4.82	5.38	4.75	5.06	6.41	4.14	4.39	4.82	5.83
U	3	1.9	2.99	1.54	1.55	1.61	1.9	2	1.94	1.64	1.4
Nb	11.7	12.6	10.4	12.4	13.1	13.8	15.5	12	12.9	12.7	12.2
Ta	0.89	0.94	0.73	0.93	1.01	1.03	1.19	0.88	0.95	0.91	0.84
Zr	114	125	109.5	117	128	129	142	117	126	122	123
Hf	3.49	3.77	3.04	3.46	3.67	3.75	4.21	3.43	3.6	3.59	3.39
La_N/Yb_N	12.12	12.69	11.79	13.23	13.07	13.65	14.2	13.1	12.34	12.64	13.68
δEu	0.68	0.61	0.67	0.6	0.6	0.63	0.67	0.58	0.65	0.69	0.72
ΣREE	101.48	109.92	92.93	101.64	111.39	110.94	132.46	99.63	102.93	107.49	113.1
LREE	93.31	101.61	84.52	94.14	103.32	103.15	123.09	92.53	95.25	99.46	104.99
HREE	8.17	8.31	8.41	7.5	8.07	7.79	9.37	7.1	7.68	8.03	8.11
LREE/HREE	11.42	12.23	10.05	12.55	12.8	13.24	13.14	13.03	12.4	12.39	12.95

Note: $\delta Eu = Eu_N/(Sm_N \times Gd_N)^{1/2}$ where N represents the normalized data of the NWA meteorites; ΣREE = LREE + HREE; LREE = La + Ce + Pr + Nd + Sm + Eu; HREE = Gd + Tb + Dy + Ho + Er + Tm + Yb + Lu.

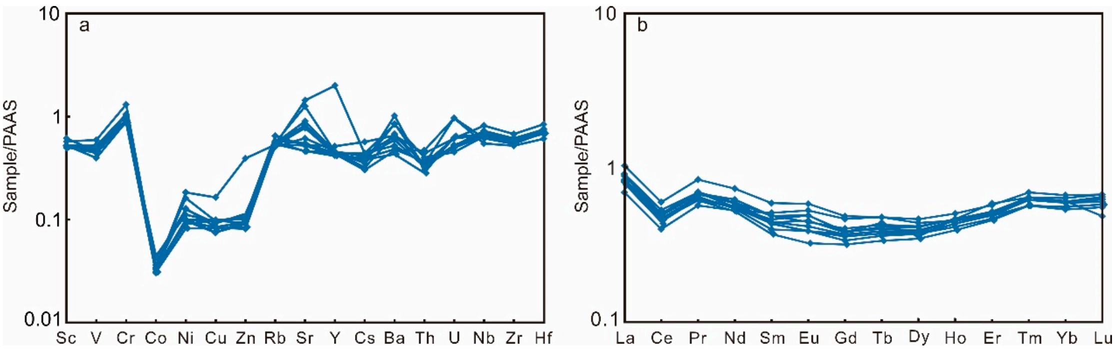

Figure 4. (**a**) PAAS-normalized spider diagram of trace element of the black shale series of the Mufushan Formation at Mufushan section; (**b**) PAAS-normalized spider diagram of REE of the black shale series of the Mufushan Formation at Mufushan section.

4.4. Characteristics of Rare Earth Elements

The results of rare earth element (REE) analysis are presented in Table 2. The light rare earth elements (LREE) represent a subgroup characterized by relatively smaller atomic numbers (La to Gd, Figure 4b). These elements are comparatively abundant within the suite of REEs and exhibit higher crustal abundances. On the other hand, the heavy rare earth elements (HREE) constitute a subgroup of REEs with relatively larger atomic numbers (Tb to Lu, Figure 4b). These elements are rarer within the REEs and display lower concentrations in the Earth's crust. The LREE/HREE ratio is an important parameter reflecting the degree of REE fractionation. If the ratio is greater than 1, it indicates enrichment of light rare earth elements (LREE) relative to heavy rare earth elements (HREE), and vice versa. In this study, all samples have L/H ($\sum$LREE/$\sum$HREE) ratios ranging from 10.05 to 13.24, with an average of 12.38, indicating enrichment of LREE relative to HREE.

After normalization to the Australian Post-Archean Average Shale (PAAS), the distribution patterns of REE in the black shale of the Mufushan Formation at the Mufushan section are shown in Figure 4b. The enrichment or depletion trends of REE in all samples are consistent, with varying degrees of depletion observed for all REE except for certain elements in a few samples (La; Figure 4b).

5. Discussion

5.1. Weathering and Sediment Recycling

Nesbitt et al. [53] demonstrated that with ongoing chemical weathering, elements such as K, Na, and Ca gradually decrease (due to feldspar weathering), while Al increases (due to the formation of clay minerals). They proposed the use of the Chemical Index of Alteration (CIA) to characterize the intensity of chemical weathering in source regions, where a higher CIA value indicates a higher degree of chemical weathering. The CIA is calculated as follows: CIA = $[Al_2O_3/(Al_2O_3 + CaO^* + Na_2O + K_2O)] \times 100$, where all quantities are expressed as molar fractions (the quantities of the involved oxides in the formula are converted to moles). CaO* represents the content of CaO in silicates. For the calculation of CaO*, Mclennan [54] proposed the following: when the molar quantity of CaO is greater than the molar quantity of Na_2O, it can be assumed that mCaO* = mNa_2O; when the molar quantity of CaO is less than the molar quantity of Na_2O, then mCaO* = mCaO.

The CIA values of the black shale in the lower part of the Mufushan Formation at the Mufushan section range from 62.3 to 66.6, with an average of 64.2 (Table 1). This indicates that the parent rocks of these black shales have undergone weak to moderately intense chemical weathering. The A-CN-K (A = Al_2O_3, CN = CaO* + Na_2O, K = K_2O) ternary relationship, as proposed by Nesbitt and Young [55,56] and Fedo et al. [57], is widely used to assess weathering in source rocks. In this diagram, the samples predominantly cluster towards illite on the A-K edge, indicating negligible influence from K-metasomatism (Figure 5a). Moreover, the parallel trend observed along the A-K edge suggests significant removal of CaO and Na_2O due to intense weathering. Parker et al. [58] was the first to propose the Weathering Index (WIP) as a method to evaluate the weathering intensity of silicate rocks by calculating the proportion of alkali and alkaline earth elements in weathering products. The WIP is defined as an index that utilizes the bond strengths of elements (K, Ca, Na, Mg) combined with oxygen as weighted factors to reflect the rock's weathering condition and its susceptibility to further weathering. The bond strength can measure the energy required to break chemical bonds and assess the relative likelihood of elements participating in weathering reactions (Nicholls, 1963). A smaller WIP value indicates a stronger weathering process. The WIP is calculated as follows: WIP = $(2Na_2O/0.35 + MgO/0.9 + 2K_2O/0.25 + CaO^*/0.7) \times 100$. Similarly, the WIP values also indicate a moderate intensity of weathering was experienced by the sediments (Figure 5b).

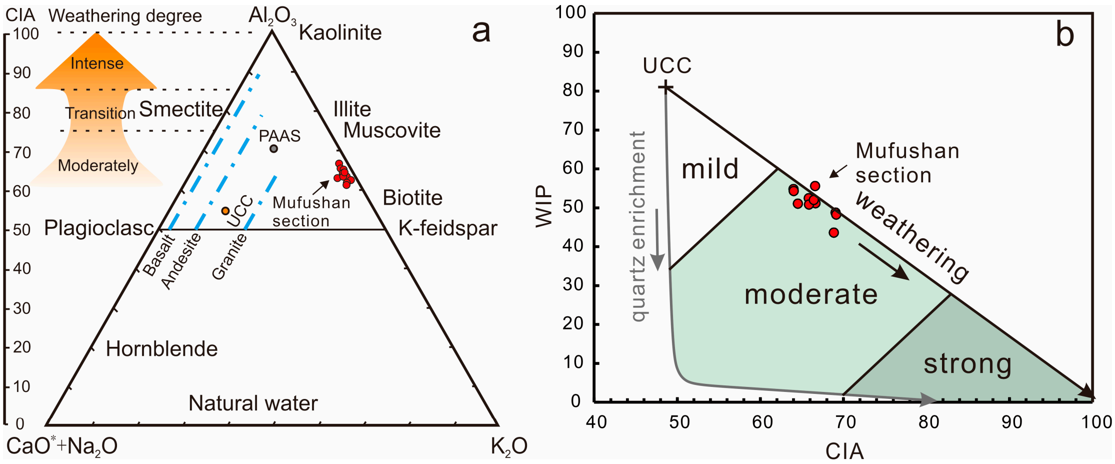

Figure 5. (**a**) A–CN–K (A = Al_2O_3, CN = CaO* + Na_2O, K = K_2O) ternary diagram suggesting predominance of Kaolinite group of minerals (modified from [56]); (**b**) Discriminating sediments with chemical indices using CIA vs. WIP plot (modified from [59]).

Thorium (Th), as an inert element, is minimally affected by hydrodynamic processes during chemical weathering and sediment formation, making it an excellent recorder of sedimentary source rock characteristics. A low Th/U ratio is consistent with a volcanic provenance that was itself derived from a depleted mantle source with low Th/U. In comparison, stable shelf sediments show highly variable Th/U ratios, commonly above 4.0. Extensive weathering can cause an increase in the Th/U ratio in sedimentary rocks, and a Th/U ratio greater than 4 is considered indicative of extensive weathering [60]. In this study, the Th/U values of all samples range from 1.673 to 4.164, with an average of 2.833. In the Th/U-Th diagram (Figure 6a), all but one sample has a Th/U ratio below 4, and lower than the average Th/U ratio of 3.8 in the upper continental crust. The majority of samples exhibit Th/U values indicating low-intensity weathering of the black shale parent rocks, while a few samples suggest moderate-intensity weathering. It should be noted that the CIA and Th/U parameters have some differences in the numerical criteria for defining the intensity of weathering, leading to slight discrepancies when using these parameters to assess the degree of weathering in samples. However, overall, both parameters indicate that the parent rocks of the black shale in the Mufushan Formation have experienced weak to moderate weathering.

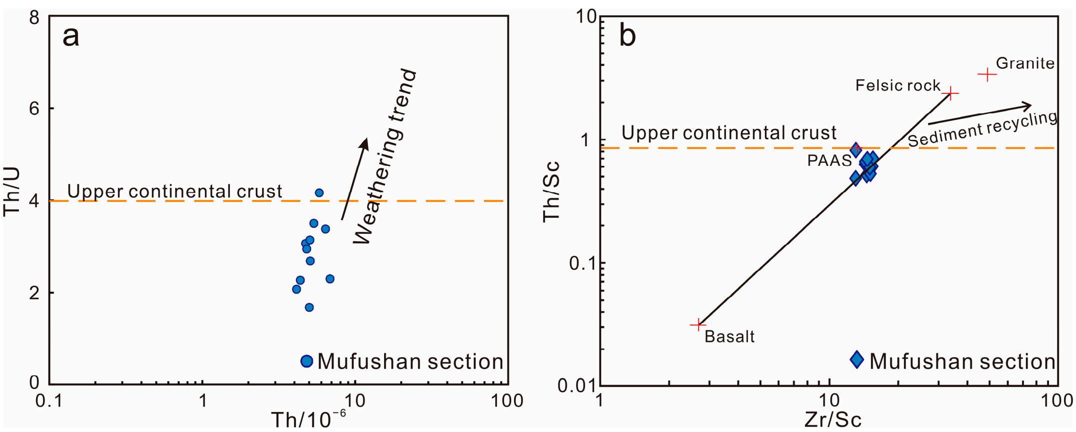

Figure 6. (**a**) Th/U-Th diagram of the black shale series of the Mufushan Formation in the Mufushan section (modified from [60]); (**b**) Th/Sc-Zr/Sc diagram of the black shale series of the Mufushan Formation in the Mufushan section (modified from [61]).

Sedimentary sorting and sedimentary recycling can lead to the enrichment of heavy minerals in sediment. The trace element Zr is commonly associated with zircon, which tends to accumulate in sediments during sorting and recycling processes due to its strong stability. On the other hand, trace elements Th and Sc are typically enriched in acidic and mafic rocks, respectively, and their concentrations remain relatively constant during sedimentary recycling. Therefore, as sedimentary sorting and recycling occur, the Th/Sc ratio remains unchanged, while the Zr/Sc ratio gradually increases [61]. Consequently, the Th/Sc-Zr/Sc diagram can be used to analyze compositional variations in sediment, the degree of sorting, and the enrichment of heavy minerals.

In the Th/Sc-Zr/Sc diagram (Figure 6b), the samples cluster near the compositional evolution line, with relatively concentrated values of Th/Sc and Zr/Sc that show minimal variation. These values are similar to those of PAAS, indicating that the detrital materials in the black shale of the lower Mufushan Formation have not undergone significant sedimentary recycling.

5.2. Source Characteristics

Based on the analysis of weathering and sedimentary recycling, it can be inferred that the source rock of the black shale in the lower Mufushan Formation of the Mufushan section has undergone weak to moderate weathering but has not experienced significant sedimentary recycling. Therefore, based on its geochemical characteristics, the source information can be accurately reconstructed, allowing for the identification of the source rock type.

The rare earth element (REE) patterns derived from the upper crust typically exhibit enrichment of LREEs, depletion of HREEs with relatively stable concentrations, and negative europium (Eu) anomalies [62]. After normalization to the chondrite values, the distribution curve of REEs in the black shale of the lower Mufushan Formation in the Mufushan section shows a pronounced rightward trend (Figure 7), indicating enrichment of LREEs relative to HREEs. Furthermore, (La/Yb)N, which is an important parameter reflecting the degree of REE fractionation, ranges from 11.79 to 14.21, with an average value of 12.95, indicating a high degree of differentiation between light and heavy REEs. The δEu value, which reflects the degree of europium fractionation relative to other REEs, ranges from 0.609 to 0.754, with an average of 0.679, indicating a negative Eu anomaly. These REE characteristics suggest that the source rock of the black shale in the lower Mufushan Formation during the early Cambrian primarily originated from the upper crust.

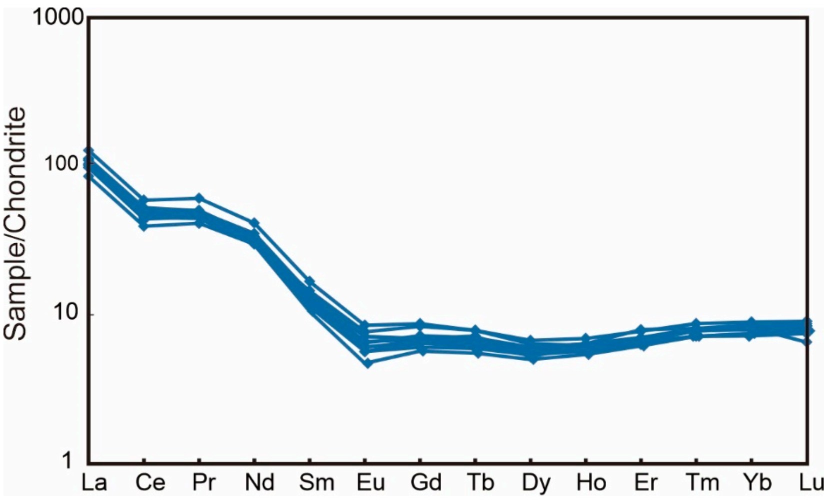

Figure 7. The REE distribution patterns of the black shale series of the Mufushan Formation in the Mufushan section.

From Table 1, it can be observed that, when compared to PAAS, the SiO_2 content of the samples is slightly higher. The Al_2O_3/(CaO + Na_2O) ratios are significantly higher than that of PAAS (Figure 8a). On the other hand, the Fe_2O_3 + MgO value is noticeably lower than that of PAAS (Figure 8b). These observations indicate that the source rock is rich in felsic rock components and lacks mafic rock components, suggesting that the source rock of the black shale in the lower Mufushan Formation during the early Cambrian tends to be felsic in nature.

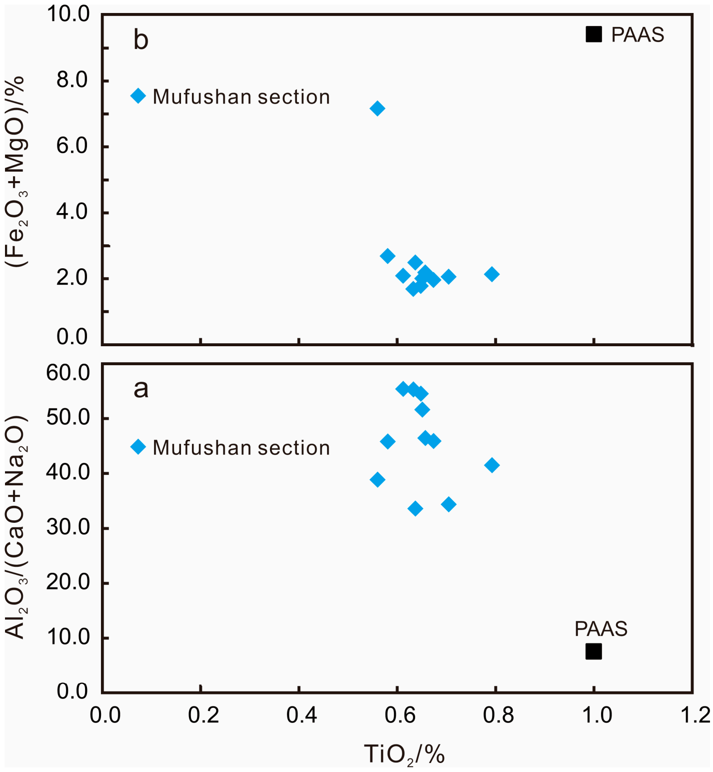

Figure 8. The eigenvalue distribution schematics of main elements of the black shale series of the Mufushan Formation in the Mufushan section. (**a**) Al_2O_3/(CaO + Na_2O)-TiO_2 diagram; (**b**) (Fe_2O_3 + MgO)-TiO_2 diagram.

A cross-plot of different data can be applied to classify the provenance of source rocks. Allegre et al. [63] proposed the use of the La/Yb-∑REE diagram to determine source rock types. In the La/Yb-∑REE diagram, the samples plot in the mixed field of granitic rocks and sedimentary rocks (Figure 9a). Floyd et al. [64] suggested the use of the La/Th-Hf diagram to identify sedimentary rock source types. In the La/Th-Hf diagram, the samples all plot in the field of mixed felsic and mafic rocks or in adjacent regions, with no samples falling within the island arc source field (Figure 9b). This suggests that the source rocks of the Mufushan Formation's black shale are not only derived by felsic rocks in the upper crust but also involve the incorporation of mafic rocks from oceanic crust. The presence of mafic rocks may be related to rift-related magmatic activity during the extensional tectonic process of the South China continent.

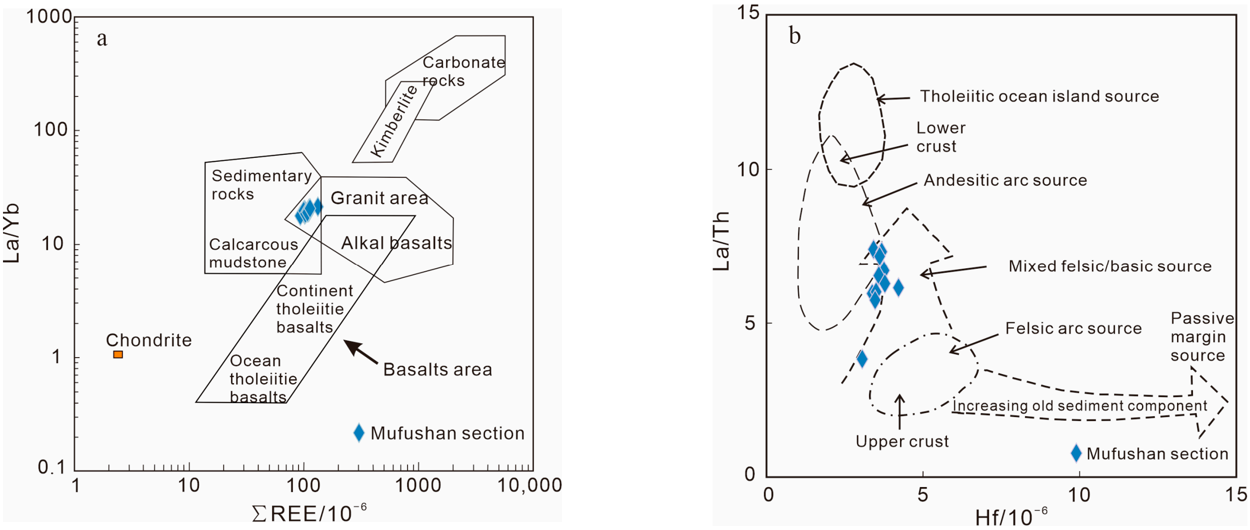

Figure 9. Discrimination diagrams for provenance attribute of the black shale series of the Mufushan Formation in the Mufushan section. (**a**) La/Yb-∑REE diagram (modified from [63]); (**b**) La/Th-Hf diagram (modified from [64]).

The above discussion indicates that the source rocks of the Mufushan Formation's basal black shale primarily consist of granitic rocks and sedimentary rocks rich in felsic minerals from the upper crust. There is also the inclusion of some mafic material. Previous studies have shown that the Yangtze Block and Cathaysia Block underwent amalgamation during the Jinning II period (850–820 Ma) and eventually formed a unified South China continent during the middle to late Neoproterozoic [21,51]. In the late Neoproterozoic, the ancient South China continent experienced extensional rifting and intracontinental rift movements in the context of the breakup of the Rodinia supercontinent. It is worth mentioning that after the assembly of the ancient South China continent in the Neoproterozoic, the extensional rifting and intracontinental rift tectonics were accompanied by rift-type magmatic activity, resulting in the formation of acidic granites and mafic-ultramafic magmatic rocks. Therefore, based on provenance characteristics and geological age relationships, it can be inferred that the granite component in the source rocks of the Lower Cambrian Mufushan Formation's black shale may be magmatic rocks formed during the Neoproterozoic magmatic activity. During the amalgamation of the Yangtze Block and the Cathaysia Block, the "Jiangnan Paleoland" (referred to as the Jiangnan Orogenic Belt in terms of continental dynamics) was formed at the southwestern margin of the study area. The "Jiangnan Paleoland", along with the "Kangdian Paleoland" and the "Cathaysia Paleoland", are considered the three major erosion zones of South China [40]. However, there have been many debates regarding the existence and timing of the formation of the "Jiangnan Paleoland" based on over half a century of research [40]. Based on the latest dating data and chronostratigraphic studies, many geologists now believe that the formation of the "Jiangnan Orogenic Belt" occurred during the Neoproterozoic (850 Ma) as a result of intracontinental orogeny during the amalgamation of the Yangtze Block and the Cathaysia Block [50]. Therefore, considering the provenance characteristics, geological age relationships, and the tectonic evolution of the South China continent, this study suggests that the provenance area of the basal black shale of the Lower Cambrian Mufushan Formation in the Lower Yangtze region was most likely the "Jiangnan Paleoland" (Jiangnan Orogenic Belt).

5.3. Source Area Tectonic Background

Sedimentary rocks in different tectonic environments exhibit variations in their rare earth element (REE) characteristics. Sediments deposited on active continental margins are typically enriched in HREEs and do not show Eu depletion. On the other hand, sediments on passive continental margins are enriched in LREEs and exhibit negative Eu anomalies. In this study, the samples show enrichment of LREEs relative to HREEs and display negative Eu anomalies. Based on these observations, it can be inferred that the tectonic environment of the source area of the basal black shale of the Mufushan Formation in the Lower Yangtze region corresponds to a passive continental margin.

Roser et al. [65] proposed that the tectonic setting of mudstone source areas can be determined using the K_2O + Na_2O-SiO_2 diagram. When plotting the shale samples from the study area on this diagram, all samples consistently fall within the passive continental margin region (Figure 10a). Mclennan et al. [66], based on the geochemical characteristics of sediments from different tectonic settings, suggested that the tectonic setting of sediment source areas can be identified using the SiO_2/Al_2O_3-K_2O/Na_2O diagram. When applying this diagram to the samples, all sample points fall within the passive continental margin region (Figure 10b). Both diagrams indicate that the source area of the basal black shale of the Mufushan Formation in the Lower Yangtze region corresponds to a passive continental margin tectonic setting.

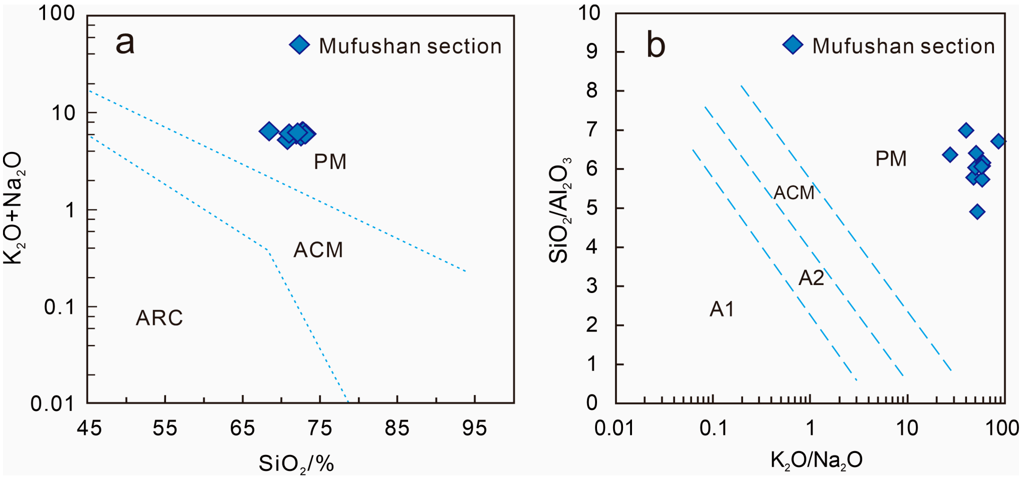

Figure 10. Discrimination diagrams for tectonic setting of main elements of the black shale series of the Mufushan Formation in the Mufushan section. (**a**) K_2O + Na_2O-SiO_2 diagram (modified from [65]); (**b**) SiO_2/Al_2O_3-K_2O/Na_2O diagram (modified from [54]); PM. Passive margin; ACM. Active continental margin; ARC. Oceanic arc; A1. Arc-related tectonics; A2. Evolving arc.

Trace elements such as La, Ce, Nd, Th, Zr, Hf, Nb, and Ti, among others, exhibit strong stability relative to major elements. They are not reactive in water and have short residence times. After initial weathering, they are incorporated into detrital sediments. Therefore, their concentrations and ratios can be used to infer the tectonic setting of the source area. Bhatia et al. [67] conducted research and proposed the use of diagrams such as La-Th-Sc, Th-Co-Zr/10, and Th-Sc-Zr/10 to determine the tectonic setting of source areas. In the La-Th-Sc diagram, all samples, except one (sample number MFS-15), fall within the vicinity of the passive continental margin (Figure 11a). In the Th-Co-Zr/10 diagram, all samples fall within the passive continental margin region (Figure 11b). In the Th-Sc-Zr/10 diagram, three samples (MFS-13, MFS-14, MFS-15) fall within the continental island arc region, while the remaining samples fall within or near the passive continental margin region (Figure 11c). Previous studies have indicated that during the early deposition of the Lower Cambrian Mufushan Formation, in the context of overall expansion of the South China continent, the scale of marine transgression increased in the Lower Yangtze region, accompanied by deepening of the seawater. Samples MFS-13, Samples MFS-14, and Samples MFS-15 are located in the upper part of the Mufushan Formation black shale, representing sediments deposited during the maximum transgressive period. At this time, the change in sedimentary environment had an impact on sediment transport and sorting. Therefore, it is inferred that the elemental characteristics of these three samples are influenced to some extent by the mixing of sediments from different sources. Considering the results from the three diagrams, it can be concluded that the source area of the basal black shale of the Mufushan Formation in the Lower Yangtze region corresponds to a passive continental margin tectonic setting.

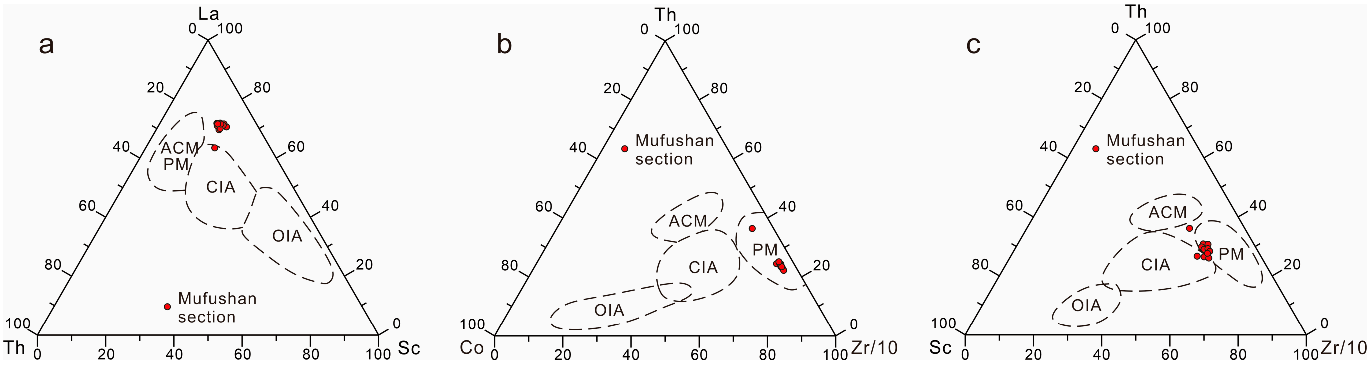

Figure 11. Discrimination diagrams for tectonic setting of trace elements of the black shale series of the Mufushan Formation in the Mufushan section (modified from [67]). (**a**) La-Th-Sc diagram; (**b**) Th-Co-Zr/10 diagram; (**c**) Th-Sc-Zr/10 diagram, PM. Passive continental margin; ACM. Active continental margin; OIA. Oceanic island arc; CIA. Continental island arc.

According to the comprehensive analysis of elemental data characteristics and discriminant diagrams, the present study reveals that the tectonic setting of the lower part of the Mufushan Formation black shale in the Lower Cambrian of the Lower Yangtze region represents a passive continental margin. Previous studies [39,46] on the geochemical features of the Lower Cambrian black shale in the Lower Yangtze region suggested that the source rocks of the black shale were formed in an active continental margin and island arc environment, which differs significantly from the conclusions of this study. By conducting comparative analysis, it is concluded that the differences in sedimentary characteristics are influenced by the mixing of sediments from different sources and changes in sedimentary environment caused by variations in water depth during the deposition period.

5.4. Paleoredox Conditions and Water Mass Restriction

Specific ratios of redox-sensitive elements such as V, Cr, Ni, Co, Mo, and U are used as redox indicators to assess the paleoredox conditions during sediment deposition. In oxidized water bodies, nickel (Ni) exists in dissolved form as ions (Ni^{2+}) or can be adsorbed by organic matter in carbonate form ($NiCO_3$) [68]. In reduced environments (in the presence of H_2S), Ni forms an insoluble sulfide (NiS), which can be slowly absorbed into solid solutions by authigenic pyrite. Cobalt (Co) is preferentially mobilized in reduced environments when compared to Ni, leading to an increase in the Ni/Co ratio in sedimentary deposits. Therefore, the Ni/Co ratio can be used to determine whether the water body was oxygen-rich or oxygen-deficient [69], with values below 5 indicating oxidized conditions, values between 5 and 7 indicating suboxic conditions, and values above 7 indicating oxygen-deficient conditions. Table 3 shows that the Ni/Co ratio of the Mufushan Formation shales ranges from 6.01 to 10.71, with an average of 8.02, indicating an oxygen-deficient environment.

Compared to Ni (nickel), V (vanadium)will preferentially precipitate from sulfide-rich environments. Therefore, when both V and Ni are simultaneously enriched, it indicates the presence of a sulfide-rich environment. The V/(V + Ni) ratio can serve as a redox indicator to infer changes in oxygen content in sedimentary environments [70]. In oxidized conditions, the V/(V + Ni) ratio is typically less than 0.45, in suboxic conditions it ranges from 0.45 to 0.60, and in oxygen-deficient conditions, it is often greater than 0.60. For the studied samples, the V/(V + Ni) ratio varies from 0.88 to 0.94, with an average of 0.92, indicating an oxygen-deficient environment.

Table 3. Trace metal data for the Mufushan Formation black shales at the Mufushan section.

Paleoredox Conditions	MFS-01	MFS-05	MFS-08	MFS-09	MFS-10	MFS-11	MFS-12	MFS-13	MFS-14	MFS-15	MFS-16
Ni/Co	6.01	6.95	7.04	7.42	7.35	8.92	10.71	6.37	7.81	6.38	13.29
V/(V + Ni)	0.93	0.93	0.90	0.93	0.93	0.92	0.91	0.94	0.93	0.93	0.88
δU	1.28	1.06	1.30	0.92	0.99	0.98	0.94	1.18	1.14	1.01	0.84
MoEF	1.61	1.99	4.00	3.83	3.92	1.50	1.66	3.28	3.23	2.53	3.07
UEF	2.03	1.11	2.15	0.99	0.95	0.96	1.00	1.23	1.20	1.00	0.92
TOC (%)	2.29	2.83	2.39	3.05	3.14	3.88	3.72	2.74	3.03	2.91	3.55

Th (thorium) and U (uranium) have different chemical properties, leading to variations in their occurrence in different environments. Th is less sensitive to redox conditions and exists in a dissolved state as Th^{4+} in water bodies. In oxygen-deficient water bodies, U forms insoluble complexes with fluoride ions as U^{4+} ions, and it readily forms organic-metal ligands in humic acids. In oxidized conditions, U exists as hexavalent U^{6+} ions and forms soluble $[UO_2(CO3)_3]^{4-}$ complexes with carbonate ions in seawater, resulting in U depletion in oxidized sedimentary environments [71]. Therefore, δU (2U/(U + Th/3)) can serve as another indicator to identify oxygen-deficient environments, where δU values > 1 indicate oxygen-deficient conditions, while values < 1 indicate oxygen-rich environments. Table 3 presents the δU values for the samples. The data indicate primarily oxygen-deficient environments, with δU values ranging from 0.84 to 1.28, and an average value of 1.06, consistent with the results mentioned earlier.

Mo (molybdenum) and U (uranium) have long residence times in the global oceans, resulting in their homogeneous distribution in water bodies [72,73]. In oxidized water, both elements exist in stable high-valence oxide forms, making them ideal indicators for reconstructing ancient marine redox conditions [74]. Due to their different behaviors in various redox zones, U's high-valence ions are reduced and enriched in denitrification environments under hypoxic conditions, and are unaffected by sulfides, while Mo mainly enriches in environments undergoing sulfate reduction [72,75,76]. Therefore, this difference in behavior allows us to differentiate the redox state of sedimentary environments [72]. The enrichment factors (EF) for Mo and U were calculated using the equation EF = (element/Al)sample/(element/Al)PAAS [52]. As shown in Table 3, for the Mufushan Formation, the U_{EF} ranges from 0.92 to 2.15, with an average of 1.23, and the Mo_{EF} ranges from 1.50 to 4.00, with an average of 2.78. Relative to the aqueous Mo_{EF}/U_{EF} ratio of present-day seawater (SW), sediment Mo_{EF}/U_{EF} ratios tend to below (~0.3 × SW) in suboxic environments, intermediate (~1 × SW) in anoxic environments, and high (~3 × SW) in strongly euxinic (sulfidic) environments Sample data points are predominantly within the range of (0.3 × SW) to (1 × SW). These values indicate hypoxic paleoredox conditions. The characteristic pattern depicted in Figure 12a, where the Mo_{EF}/U_{EF} ratio decreases with increasing U_{EF}, is similar to modern Black Sea sediments. This trend reflects a stagnant environment.

The Mo/TOC ratio can be used to assess the confinement degree of water bodies [77]. In restricted deep-water basins, the removal rate of Mo from seawater exceeds its supply rate, leading to Mo depletion in seawater and a gradual decrease in Mo content in sediments, as seen in environments like the Black Sea. In contrast, in open ocean basins, Mo continuously receives replenishment from the global ocean, resulting in Mo concentrations approaching the average value of global seawater. As shown in Figure 12b, the Mo/TOC ratio of the samples in the study area is lower than that of Black Sea sediments, indicating that they were deposited in a basin with a higher confinement degree.

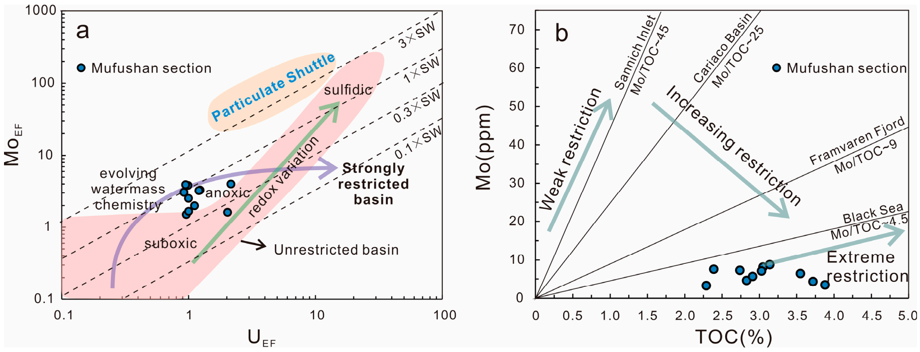

Figure 12. (**a**) Mo_{EF} versus U_{EF} in samples from the Mufushan Formations. The post-Archean average shale (PAAS) composition data used in this study are from Taylor and McLennan (1985) [52]. The interpretation lines are from Algeo and Tribovillard (2009) [72] and Tribovillard et al. (2012) [77]; (**b**) Mo (ppm) versus TOC (%) in samples from the Mufushan formations. The interpretation lines are from Algeo and Lyons (2006) [78].

6. Conclusions

(1) The CIA and Th/U indices indicate that the basal black shale of the Mufushan Formation in the Mufushan section has undergone weak to moderate weathering. The Th/Sc-Zr/Sc diagram suggests that the sedimentary detrital material of the black shale has not undergone sedimentary recycling. Therefore, the geochemical characteristics of the black shale can effectively indicate the composition of the source rocks.

(2) The distribution patterns of rare earth elements, as well as parameters such as (La/Yb)N and δEu, indicate that the source rocks of the black shale in the study area are mainly derived from the upper crust. By analyzing the content or ratios of various major elements such as SiO_2, Fe_2O_3 + MgO, Al_2O_3/(CaO + Na_2O) in the samples, and their positions in the La/Yb-∑REE and La/Th-Hf diagrams, it is inferred that the source rocks of the basal black shale of the Mufushan Formation mainly consist of granites and sedimentary rocks rich in ferromagnesian minerals, which belong to the upper crustal felsic rocks. There is also evidence of the involvement of mafic rocks, although no island arc volcanic rock source is identified. Based on the source rock characteristics and geological age relationships, it can be inferred that the granite component in the source rocks of the black shale represents magmatic rocks formed during the Neoproterozoic. Considering the tectonic evolution of the South China continent, it is believed that the source area of the basal black shale of the Mufushan Formation in the Lower Yangtze region corresponds to the "Jiangnan Ancient Land" (Jiangnan Orogenic Belt).

(3) The content of light and heavy rare earth elements in the samples, as well as the elemental characteristics of Eu and their positions in various diagrams such as K_2O + Na_2O-SiO_2, K_2O/Na_2O-SiO_2/Al_2O_3, La-Th-Sc, Th-Co-Zr/10, Th-Sc-Zr/10, indicate that the source area of the basal black shale of the Lower Cambrian Mufushan Formation in the Lower Yangtze region corresponds to a stable tectonic setting of a passive continental margin.

(4) The redox-sensitive elements examined in this study provide valuable insights into the redox conditions and environmental settings during the deposition of the Mufushan Formation. The Ni/Co ratio, V/(V + Ni) ratio, δU values, and Mo_{EF}/U_{EF} ratios collectively suggest the prevalence of oxygen-deficient conditions in the sedimentary environment. This is further supported by the Mo/TOC ratio, indicating a higher confinement degree for the depositional basin.

Author Contributions: Conceptualization, methodology, investigation, data curation, writing—original draft preparation, J.L.; writing—review and editing, Z.K. (Zhihong Kang); visualization, X.Z.; supervision, project administration, funding acquisition, Z.K. (Zhijiang Kang). All authors have read and agreed to the published version of the manuscript.

Funding: This work was supported by the Joint Fund for Enterprise Innovation and Development of National Natural Science Foundation of China (Grant number U19B6003).

Institutional Review Board Statement: Not applicable.

Informed Consent Statement: Not applicable.

Data Availability Statement: Data available on request from the authors.

Conflicts of Interest: The authors declare no conflict of interest.

References

1. Wu, T.; Yang, R.; Gao, L.; Li, J.; Gao, J. Origin and Enrichment of Vanadium in the Lower Cambrian Black Shales, South China. *ACS Omega* **2021**, *6*, 26870–26879. [CrossRef]
2. Hao, Y.; Liu, H.; Chen, Q.; Sun, W.; Huang, J. Redox-sensitive elements of Ediacaran black shales in South China with implications for a widespread anoxic ocean. *J. Asian Earth Sci.* **2023**, *251*, 105670. [CrossRef]
3. Martins, G.G.; Mendes, J.C.; Schmitt, R.d.S.; Armstrong, R.; Vieira, T.A.T. Long-term magmatism in the Ribeira Orogen, Western Gondwana: SHRIMP U-Pb and O isotope data for two Ediacaran-Cambrian magmatic events in the Rio de Janeiro area. *Precambrian Res.* **2022**, *383*, 106908. [CrossRef]
4. Ding, Y.; Sun, W.; Liu, S.; Xie, J.; Tang, D.; Zhou, X.; Zhou, L.; Li, Z.; Song, J.; Li, Z.; et al. Low oxygen levels with high redox heterogeneity in the late Ediacaran shallow ocean: Constraints from I/(Ca plus Mg) and Ce/Ce* of the Dengying Formation, South China. *Geobiology* **2022**, *20*, 790–809. [CrossRef]
5. He, J.Y.; Qing, H.R.; Xu, B. The unconformity-related palaeokarst in the uppermost Ediacaran carbonate rocks in the northwestern Tarim Block, NW China: Implication for sedimentary evolution during the Ediacaran-Cambrian transition. *Int. Geol. Rev.* **2019**, *61*, 839–852. [CrossRef]
6. Li, W.P.; Zheng, Y.F.; Zhao, Y.Y. Geochemical evidence from marine carbonate for enhanced terrigenous input into seawater during the Ediacaran-Cambrian transition in South China. *Precambrian Res.* **2017**, *291*, 83–97. [CrossRef]
7. Zhang, S.-H.; Ernst, R.E.; Yang, Z.; Zhou, Z.; Pei, J.; Zhao, Y. Spatial distribution of 1.4-1.3 Ga LIPs and carbonatite-related REE deposits: Evidence for large-scale continental rifting in the Columbia (Nuna) supercontinent. *Earth Planet. Sci. Lett.* **2022**, *597*, 117815. [CrossRef]
8. Ribeiro, B.V.; Lopes, L.B.L.; Kirkland, C.L.; Cawood, P.A.; Faleiros, F.M.; Hartnady, M.I.H.; Teixeira, W.; Mulder, J.A.; Roberts, N.M.W.; Tassinari, C.C.G. Growing the Paleo- to Mesoproterozoic margin of the SW Amazonia and the transition from an accretionary to a collisional system. *Precambrian Res.* **2022**, *381*, 106841. [CrossRef]
9. Jana, N.; Singh, C.; Singh, A.; Eken, T.; Dubey, A.K.; Dutta, A.; Gupta, A.K. Lithospheric architecture below the Eastern Ghats Mobile Belt and adjoining Archean cratons: Imprints of India-Antarctica collision tectonics. *Gondwana Res.* **2022**, *111*, 209–222. [CrossRef]
10. Neogi, S.; Bhardwaj, A.; Kundu, A. Evolution of Neoproterozoic Shillong Basin, Meghalaya, NE India: Implications of supercontinent break-up and amalgamation. *Geol. Mag.* **2022**, *159*, 628–644. [CrossRef]
11. Teng, X.; Zhang, J.; Mao, X.; Lu, Z.; Zhou, G.; Wu, Y.; Guo, Q. Qaidam block situated in the interior of Rodinia and Gondwana: New magmatic and metamorphic constraints. *Precambrian Res.* **2022**, *381*, 106866. [CrossRef]
12. Neves, S.P. Comparative geological evolution of the Borborema Province and Sao Francisco Craton (eastern Brazil): Decratonization and crustal reworking during West Gondwana assembly and implications for paleogeographic reconstructions. *Precambrian Res.* **2021**, *355*, 106119. [CrossRef]
13. Wang, W.; Cawood, P.A.; Pandit, M.K.; Xia, X.; Raveggi, M.; Zhao, J.; Zheng, J.; Qi, L. Fragmentation of South China from greater India during the Rodinia-Gondwana transition. *Geology* **2021**, *49*, 228–232. [CrossRef]
14. Jing, X.; Evans, D.A.D.; Yang, Z.; Tong, Y.; Xu, Y.; Wang, H. Inverted South China: A novel configuration for Rodinia and its breakup. *Geology* **2021**, *49*, 463–467. [CrossRef]
15. Dan, W.; Murphy, J.B.; Tang, G.-J.; Zhang, X.-Z.; White, W.M.; Wang, Q. Cambrian-Ordovician magmatic flare-up in NE Gondwana: A silicic large igneous province? *Geol. Soc. Am. Bull.* **2023**, *135*, 1618–1632. [CrossRef]
16. Zhang, Y.; Sun, M.; Yin, J.; Yuan, C.; Sun, Z.; Xia, X. Subduction initiation of the western Paleo-Asian Ocean linked to global tectonic reorganization: Insights from Cambrian island-arc magmatism within the West Junggar, NW China. *Geol. Soc. Am. Bull.* **2022**, *134*, 3099–3112. [CrossRef]
17. Yang, C.; Li, X.-H.; Zhu, M.-Y. Tectonic regime transition of the western South China Block in early Cambrian: Evidence from the Meishucun volcanic ash beds. *Palaeoworld* **2022**, *31*, 591–599. [CrossRef]

18. Arenas, R.; Rojo-Perez, E.; Diez Fernandez, R.; Albert, R.; Novo-Fernandez, I.; Sanchez Martinez, S.; Fuenlabrada, J.M.; Andonaegui, P.; Moreno-Martin, D.; Gerdes, A.; et al. Opening and closure of Cadomian peri-Gondwanan oceans: Age and evolution of the Merida Ophiolite (SW Iberia). *Int. Geol. Rev.* **2022**, *16*, 210–221. [CrossRef]
19. Karsli, O.; Sengun, F.; Dokuz, A.; Aydin, F.; Kandemir, R.; Kristoffersen, M.; Santos, J.F.; Hofmann, M.; Duygu, L. Early Cambrian S-type granites in the Sakarya Zone, NE Turkey: A record for transition from subduction to post-collisional extension deduced from U-Pb zircon age and Nd-Hf isotopes. *Lithos* **2022**, *428*, 106809. [CrossRef]
20. Dong, Y.; Cao, S.; Zhan, L.; Li, W.; Neubauer, F.; Genser, J. Tectono-magmatism evolution in the Gaoligong orogen belt during Neoproterozoic to Paleozoic: Significance for assembly of East Gondwana. *Precambrian Res.* **2022**, *378*, 106776. [CrossRef]
21. Wang, X.; Zhang, J.; Shi, M.; Pang, Y.; Zhao, Y.; Yang, X. Changing Hydrocarbon-Producing Potential of the Cambrian Niutitang Shale: Insights from Pyrite Morphology and Geochemical Characteristics. *ACS Omega* **2023**, *8*, 7172–7190. [CrossRef] [PubMed]
22. Liu, P.; Liu, C.J.; Guo, R.L. Depositional Environment and Organic Matter Enrichment in the Lower Paleozoic Shale from the Northeastern Margin of the Yangtze Platform, South China. *J. Mar. Sci. Eng.* **2023**, *11*, 18. [CrossRef]
23. Chen, X.; Shields, G.A.; Andersen, M.B.; Qiu, C.; Min, S.Y.; Shao, Q.-F.; Ling, H.-F. Oceanic redox conditions during the terminal Cambrian extinction event. *Chem. Geol.* **2023**, *626*, 121456. [CrossRef]
24. Zhao, K.; Zhu, G.; Li, T.; Chen, Z.; Li, S. Fluctuations of continental chemical weathering control primary productivity and redox conditions during the Earliest Cambrian. *Geol. J.* **2023**, *1*, 1–14. [CrossRef]
25. Wu, X.; Luo, H.; Zhang, J.; Chen, Q.; Fang, X.; Wang, W.; Li, W.; Shi, Z.; Zhang, Y. Volcanism-driven marine eutrophication in the end-Ordovician: Evidence from radiolarians and trace elements of black shale in South China. *J. Asian Earth Sci.* **2023**, *253*, 105687. [CrossRef]
26. Cherry, L.B.; Gilleaudeau, G.J.; Grazhdankin, D.V.; Romaniello, S.J.; Martin, A.J.; Kaufman, A.J. A diverse Ediacara assemblage survived under low-oxygen conditions. *Nat. Commun.* **2022**, *13*, 7306. [CrossRef]
27. Yang, H.; Yang, L.; Zhou, M. Expanded deepwater euxinia recorded in the Ediacaran-Cambrian boundary interval in South China. *J. Asian Earth Sci.* **2022**, *230*, 105192. [CrossRef]
28. Zhuravlev, A.Y.; Mitchell, E.G.; Bowyer, F.; Wood, R.; Penny, A. Increases in reef size, habitat and metacommunity complexity associated with Cambrian radiation oxygenation pulses. *Nat. Commun.* **2022**, *13*, 7523. [CrossRef]
29. Peng, M.H.; Ma, D.Q.; Tian, J.C.; Zhang, X.; Li, J. Paleoenvironmental changes during the Middle-Late Ordovician transition, Northwestern Tarim Basin, NW China and implications for the great Ordovician Biodiversification Event. *J. Asian Earth Sci.* **2023**, *242*, 17. [CrossRef]
30. Fu, X.; Xu, L.; Yan, H.; Ye, H.; Ding, J. Mineralogy and trace element geochemistry of the early Cambrian black shale-hosted Zhongcun vanadium deposit, southern Qinling, China. *Ore Geol. Rev.* **2023**, *155*, 105371. [CrossRef]
31. Wang, Z.; Tan, J.; Hilton, J.; Dick, J.; Wen, Z. Trace element enrichment mechanisms in black shales during the early cambrian (ca. 521–514 Ma), South China. *Mar. Pet. Geol.* **2023**, *149*, 106083. [CrossRef]
32. Tian, T.; Yao, J.; Guo, W.; Duan, Z.; Fu, D.; Yang, F. Provenance and Tectonic Setting Discrimination and Their Effects on the Pore-Scale Fluid Flow of Black Shale: Take the Micangshan Tectonic Belt, Central China, as an Example. *Geofluids* **2023**, *2023*, 9207960. [CrossRef]
33. Ning, S.; Xia, P.; Zou, N.; Zhong, Y.; Yu, Y.; Mou, Y.; Wang, K. Organic matter pore characteristics of over-mature marine black shale: A comparison of organic fractions with different densities. *Front. Earth Sci.* **2023**, *17*, 310–321. [CrossRef]
34. Zhang, L.; Wang, H.; Dong, D.; Zhao, Q.; Wu, C. Gravity-flow deposits and implications for unconventional oil and gas in the Ordovician-Silurian Wufeng-Longmaxi Formation, Sichuan Basin, South China. *AAPG Bull.* **2023**, *107*, 957–988. [CrossRef]
35. Ding, J.; Sun, J.; Nie, H.; Yang, X.; Ye, Y.; Shi, G.; Wang, R.; Huang, B.; Sun, X.; Li, H. Organic Geochemical Characteristics and Organic Matter Enrichment of the Upper Permian Longtan Formation Black Shale in Southern Anhui Province, South China. *ACS Omega* **2023**, *8*, 16748–16761. [CrossRef] [PubMed]
36. Cai, Q.S.; Hu, M.Y.; Kane, O.I.; Yang, Z.; Wen, Y.R.; Luo, Q.; Li, M.T.; Hu, Z.G.; Deng, Q.J. Petrological and geochemical characteristics of the Ordovician-Silurian black shale in eastern Sichuan and western Hubei, South China: Differential sedimentary responses to tectonism and glaciation. *J. Palaeogeogr.-Engl.* **2023**, *12*, 129–152. [CrossRef]
37. Zhang, C.; Fang, C.; Zhao, Q.; Meng, G.; Zhou, D.; Li, J.; Shao, W. Multi-Proxies Analysis of Organic Matter Accumulation of the Late Ordovician-Early Silurian Black Shale in the Lower Yangtze Region, South China. *Minerals* **2023**, *13*, 400. [CrossRef]
38. Ding, J.; Sun, J.; Nie, H.; Yang, X.; Ye, Y.; Shi, G.; Wang, R.; Huang, B.; Li, H. Application of biomarkers in characterization of organic matter source, maturity and palaeoredox condition of black shales from the upper Permian Dalong Formation in Southern Anhui Province, South China. *Geol. J.* **2023**, *58*, 1741–1759. [CrossRef]
39. Ding, M.; Li, Y.; Fan, T.; Lash, G.; Wei, X.; Zhang, T. Geochemistry of the Lower Silurian black shales from the Upper Yangtze Platform, South China: Implications for paleoclimate, provenance, and tectonic setting. *J. Asian Earth Sci.* **2023**, *242*, 105493. [CrossRef]
40. Zhang, Q.; Zhang, B.; Yu, Q.; Men, Y.; Zhang, H.; Kang, J.; Cao, J.; Zhao, A.; Zhou, Y.; Feng, X. Study on the Provenance and Tectonic Setting of Mudstone in the Lower Silurian Longmaxi Formation of the Yanyuan Basin on the Western Margin of the Yangtze Platform. *Minerals* **2023**, *13*, 194. [CrossRef]
41. Jiang, F.; Chen, D.; Zhu, C.; Ning, K.; Ma, L.; Xu, T.; Qin, R.; Li, B.; Chen, Y.; Huo, L.; et al. Mechanisms for the anisotropic enrichment of organic matter in saline lake basin: A case study of the Early Eocene Dongpu Depression, eastern China. *J. Pet. Sci. Eng.* **2022**, *210*, 110035. [CrossRef]

42. Shi, J.; Zou, Y.R.; Cai, Y.L.; Zhan, Z.W.; Sun, J.N.; Liang, T. Organic matter enrichment of the Chang 7 member in the Ordos Basin: Insights from chemometrics and element geochemistry. *Mar. Pet. Geol.* **2022**, *135*, 105404. [CrossRef]
43. Wang, Y.; Chen, J.; Shen, W.; Li, M. Mechanism of Organic Matter Accumulation in Black Shales of the Yuertusi Formation in the Tarim Basin: Insights From Paleoenvironmental Variation during the Early Cambrian. *Front. Earth Sci.* **2022**, *10*, 879658. [CrossRef]
44. Decree, S.; Pasava, J.; Baele, J.-M.; Mercadier, J.; Roesel, D.; Frimmel, H. In-situ trace element and Sr isotope signature of apatite: A new key to unravelling the genesis of polymetallic mineralisation in black shales of the Early Cambrian Niutitang Formation, Southern China. *Ore Geol. Rev.* **2022**, *150*, 105130. [CrossRef]
45. Zhang, Q.; Men, Y.; Yu, Q.; Wang, G.; Xiao, Y.; Zhang, H.; Zhao, A.; Zhou, Y.; Cao, J. Characteristics and Enrichment Genesis of the Platinum Group Elements (PGEs) in Organic Rich Shale of the Wufeng and Longmaxi Formations of upper Ordovician and Lower Silurian in the Sichuan Basin. *Minerals* **2022**, *12*, 1363. [CrossRef]
46. Yu, M.; Ye, Z.; Jiaxi, Z.; Yufeng, T.; Liang, W.; Shizhong, L.; Yaotang, Z.; Wanneng, W. The Origin of the Black Shale Series and Bentonites from the Wufeng Formation in the Southwestern Upper Yangtze: Implications for the Convergence of the Yangtze and Cathaysia Blocks in the Late Ordovician. *Acta Geol. Sin.-Engl. Ed.* **2022**, *96*, 1897–1916. [CrossRef]
47. Zhang, G.; Chen, D.; Ding, Y.; Huang, T. Controls on Organic Matter Accumulation from an Upper Slope Section on the Early Cambrian Yangtze Platform, South China. *Minerals* **2023**, *13*, 260. [CrossRef]
48. Liu, Z.; Yan, D.; Yuan, D.; Niu, X.; Fu, H. Multiple controls on the organic matter accumulation in early Cambrian marine black shales, middle Yangtze Block, South China. *J. Nat. Gas Sci. Eng.* **2022**, *100*, 104454. [CrossRef]
49. Fu, Y.; Wang, F.; Guo, C.; Li, C.; Xia, P. Re-Os Geochronology of the Liuchapo Formation across the Ediacaran-Cambrian Boundary of the Yangtze Block (South China). *J. Earth Sci.* **2022**, *33*, 25–35. [CrossRef]
50. Shi, Z.; Zhao, S.; Zhou, T.; Ding, L.; Sun, S.; Cheng, F. Mineralogy and Geochemistry of the Upper Ordovician and Lower Silurian Wufeng-Longmaxi Shale on the Yangtze Platform, South China: Implications for Provenance Analysis and Shale Gas Sweet-Spot Interval. *Minerals* **2022**, *12*, 1190. [CrossRef]
51. Zhang, J.; Fan, T.; Algeo, T.J.; Li, Y.; Zhang, J. Paleo-marine environments of the Early Cambrian Yangtze Platform. *Palaeogeogr. Palaeoclimatol. Palaeoecol.* **2016**, *256*, 130–155. [CrossRef]
52. McLennan, S.M.; Taylor, S.R. *The Continental Crust: Its Composition and Evolution*; Blackwell Scientific Pub.: Palo Alto, CA, USA, 1985.
53. Nesbitt, H.W.; Young, G.M. Early Proterozoic Climates and Plate Motions Inferred from Major Element Chemistry of Lutites. *Nature* **1982**, *299*, 715–717. [CrossRef]
54. McLennan, S.M. Weathering and global denudation. *J. Geol.* **1993**, *101*, 295–303. [CrossRef]
55. Nesbitt, H.W.; Young, G.M. Formation and diagenesis of weathering profiles. *J. Geol.* **1989**, *97*, 129–147. [CrossRef]
56. Nesbitt, H.W.; Young, G.M. Prediction of some weathering trends of plutonic and volcanic rocks based on thermodynamic and kinetic considerations. *Geochim. Cosmochim. Acta* **1984**, *48*, 1523–1534. [CrossRef]
57. Fedo, C.M.; Wayne Nesbitt, H.; Young, G.M. Unraveling the effects of potassium metasomatism in sedimentary rocks and paleosols, with implications for paleoweathering conditions and provenance. *Geology* **1995**, *23*, 921–924. [CrossRef]
58. Parker, A. An index of weathering for silicate rocks. *Geol. Mag.* **1970**, *107*, 501–504. [CrossRef]
59. Garzanti, E.; Padoan, M.; Setti, M.; Najman, Y.; Peruta, L.; Villa, I.M. Weathering geochemistry and Sr-Nd fingerprints of equatorial upper Nile and Congo muds. *Geochem. Geophys. Geosyst.* **2013**, *14*, 292–316. [CrossRef]
60. McLennan, S.M.; Hemming, S.R.; Taylor, S.R.; Eriksson, K.A. Early proterozoic crustal evolution—Geochemical and ND-PB isotopic evidence from metasedimentary rocks, southwestern North-America. *Geochim. Cosmochim. Acta* **1995**, *59*, 1153–1177. [CrossRef]
61. Lambeck, A.; Huston, D.; Maidment, D.; Southgate, P. Sedimentary geochemistry, geochronology and sequence stratigraphy as tools to typecast stratigraphic units and constrain basin evolution in the gold mineralised Palaeoproterozoic Tanami Region, Northern Australia. *Precambrian Res.* **2008**, *166*, 185–203. [CrossRef]
62. McLennan, S.M. *Rare-Earth Elements in Sedimentary-Rocks—Influence of Provenance and Sedimentary Processes*; Mineralogical Soc America: Washington, DC, USA, 1989; Volume 21, pp. 169–200.
63. Allègre, C.J.; Minster, J.F. Quantitative models of trace element behavior in magmatic processes. *Earth Planet. Sci. Lett.* **1978**, *38*, 1–25. [CrossRef]
64. Floyd, P.A.; Leveridge, B.E. Tectonic environment of the devonian gramscatho BASIN, south cornwall–Framework mode and geochemical evidence from turbiditic sandstones. *J. Geol. Soc.* **1987**, *144*, 531–542. [CrossRef]
65. Roser, B.P.; Korsch, R.J. Determination of tectonic setting of sandstone-mudstone suites using SiO_2 content and K_2O Na_2O ratio. *J. Geol.* **1986**, *94*, 635–650. [CrossRef]
66. Mclennan, S.M.; Hemming, S.R.; Mcdaniel, D.K.; Hanson, G.N. *Geochemical Approaches to Sedimentation, Provenance, and Tectonics*; Processes Controlling the Composition of Clastic Sediments; Geological Society of America: Boulder, CO, USA, 1993; Volume 284.
67. Bhatia, M.R.; Crook, K.A.W. Trace-element characteristics of graywackes and tectonic setting discrimination of sedimentary basins. *Contrib. Mineral. Petrol.* **1986**, *92*, 181–193. [CrossRef]
68. Calvert, S.E.; Pedersen, T.F. Geochemistry of recent oxic and anoxic marine-sediments–Implications for the geological record. *Mar. Geol.* **1993**, *113*, 67–88. [CrossRef]

69. Jones, B.; Manning, D.A.C. Comparison of geochemical indexes used for the interpretation of palaeoredox conditions in ancient Mudstones. *Chem Geol* **1994**, *111*, 111–129. [CrossRef]
70. Arthur, M.A.; Sageman, B.B. Marine black shales—Depositional mechanisms and environments of ancient-deposits. *Annu. Rev. Earth Planet. Sci.* **1994**, *22*, 499–551. [CrossRef]
71. Algeo, T.J.; Maynard, J.B. Trace-element behavior and redox facies in core shales of Upper Pennsylvanian Kansas-type cyclothems. *Chem. Geol.* **2004**, *206*, 289–318. [CrossRef]
72. Algeo, T.J.; Tribovillard, N. Environmental analysis of paleoceanographic systems based on molybdenum-uranium covariation. *Chem. Geol.* **2009**, *268*, 211–225. [CrossRef]
73. Tribovillard, N.; Algeo, T.J.; Lyons, T.; Riboulleau, A. Trace metals as paleoredox and paleoproductivity proxies: An update. *Chem. Geol.* **2006**, *232*, 12–32. [CrossRef]
74. Wei, Y.; Li, X.; Zhang, R.; Li, X.; Lu, S.; Qiu, Y.; Jiang, T.; Gao, Y.; Zhao, T.; Song, Z.; et al. Influence of a Paleosedimentary Environment on Shale Oil Enrichment: A Case Study on the Shahejie Formation of Raoyang Sag, Bohai Bay Basin, China. *Front. Earth Sci.* **2021**, *9*, 736054. [CrossRef]
75. Zheng, Y.; Anderson, R.F.; van Geen, A.; Kuwabara, J. Authigenic molybdenum formation in marine sediments: A link to pore water sulfide in the Santa Barbara Basin. *Geochim. Cosmochim. Acta* **2000**, *64*, 4165–4178. [CrossRef]
76. Wang, C.; Wang, Q.; Chen, G.; He, L.; Xu, Y.; Chen, L.; Chen, D. Petrographic and geochemical characteristics of the lacustrine black shales from the Upper Triassic Yanchang Formation of the Ordos Basin, China: Implications for the organic matter accumulation. *Mar. Pet. Geol.* **2017**, *86*, 52–65. [CrossRef]
77. Algeo, T.J.; Morford, J.; Cruse, A. Reprint of: New Applications of Trace Metals as Proxies in Marine Paleoenvironments. *Chem. Geol.* **2012**, *324*, 1–5. [CrossRef]
78. Algeo, T.J.; Lyons, T.W. Mo-total organic carbon covariation in modern anoxic marine environments: Implications for analysis of paleoredox and paleohydrographic conditions. *Paleoceanography* **2006**, *21*, 16–23. [CrossRef]